Structured Light Generation Using Angle-Multiplexed Metasurfaces

Lin Deng, Renchao Jin, Yihao Xu, and Yongmin Liu*

On the basis of the Jones matrix, independent control over the amplitude and phase of light has been demonstrated by combining several meta-atoms into the supercell of a metasurface. However, due to the intrinsic limitation of a planar achiral structure, the maximum number of independent, complex elements in one Jones matrix is three, giving rise to up to three-channel amplitude and phase control. In this work, more Jones matrices corresponding to different angles of incidence are proposed to add, so that the degrees of freedom in the amplitude and phase control can be further increased. The supercell of the designed metasurfaces consists of three dielectric nanoblocks with predefined rotation angles and displacements in the 2D space, which can be inversely determined with the help of the genetic algorithm. Empowered by the ability to realize four- or even eight-channel amplitude and phase control, the generation of multiple structured light, including two independent perfect Poincaré beams, two double-ring perfect Poincaré beams, two perfect Poincaré beam arrays, and four vector vortex beam arrays, is numerically demonstrated. Such novel designs are expected to benefit the development of modern optical applications, including but not limited to optical communications, quantum information, and signal encryption.

1. Introduction

Metasurfaces,[1–8] which are composed of 2D subwavelength meta-atoms, have drawn wide attention in the past decade because of their compact size and novel functionalities. Various devices with the same or more complicated functions compared to the bulky optical counterparts have been reported based on distinct metasurfaces, such as focal lenses,[9–11] polarizers,[12–14] vortex beam generators,[15–17] holograms,[18–20] and spot projection.[21–23] However, in previously reported metasurfaces, the unit cell typically consists of a single meta-atom, hence the output degrees of freedom (DOF) are restrained by

a simple Jones matrix. To further increase the DOF of metasurfaces, researchers have recently proposed to integrate several meta-atoms with varying geometric parameters into a supercell. On the basis of this methodology, applications such as arbitrary polarization generation, on-demand polarization conversion, and multiplexing nanoprinting and holograms have been reported.[24–34] With the ability to match the complex electric fields for each of the multiplexing channels, these designs have shown their advantages of large information capacity, high imaging quality, and precise wavefront control. Up to six DOF in the combined Jones matrix, which is the theoretical upper limit corresponding to the amplitude and phase (AP) control of the three elements in the Jones matrix for planar achiral metasurfaces, have been successfully realized with the help of the genetic algorithm (GA).[34] Very recently, Xiong et al. have demonstrated that multiple polarization channels can be independently controlled by introducing correlated and noncorrelated noise to the Jones matrix elements with complex values.[35] Up to 11 polarization channels and 36 holographic images have been realized, while the total intrinsic DOF of this single Jones matrix are still 6.

Although the maximum DOF in a single Jones matrix were demonstrated, it is still possible to surpass this limit and further expand the AP control channels. For conventional metasurface design,[1,36–39] light is usually illuminated perpendicular to the metasurfaces plane, and the optical responses recorded are typically carried by zero-order transmitted or reflected light (i.e., without diffraction). The angle of incidence and high-order diffracted beams can be taken into account to add extra DOF in the design. One possible way is to design metasurfaces with variable geometries that can have different resonant modes and thus independent phase control in response to the angles of incidence.[40,41] However, the total optical DOF of the metasurfaces produced by the brute-force parameter sweeping method is still constrained since the permitted resonant modes are not always able to cover the entire complex amplitude space, particularly when a number of polarization states and angles are involved. Another method is to utilize light at different diffraction angles for multiplxing,[42,43] so that various functions can be engineered for different high-order diffracted beams. Moreover, when the direction of incidence is changed, multiple functions can be realized at a fixed observation angle, for example, along the direction perpendicular

L. Deng, Y. Liu
Department of Electrical and Computer Engineering
Northeastern University
Boston, MA 02115, USA
E-mail: y.liu@northeastern.edu
R. Jin, Y. Xu, Y. Liu
Department of Mechanical and Industrial Engineering
Northeastern University
Boston, MA 02115, USA

The ORCID identification number(s) for the author(s) of this article can be found under https://doi.org/10.1002/adom.202300299

**ADVANCED
SCIENCE NEWS**

www.advancedsciencenews.com

**ADVANCED
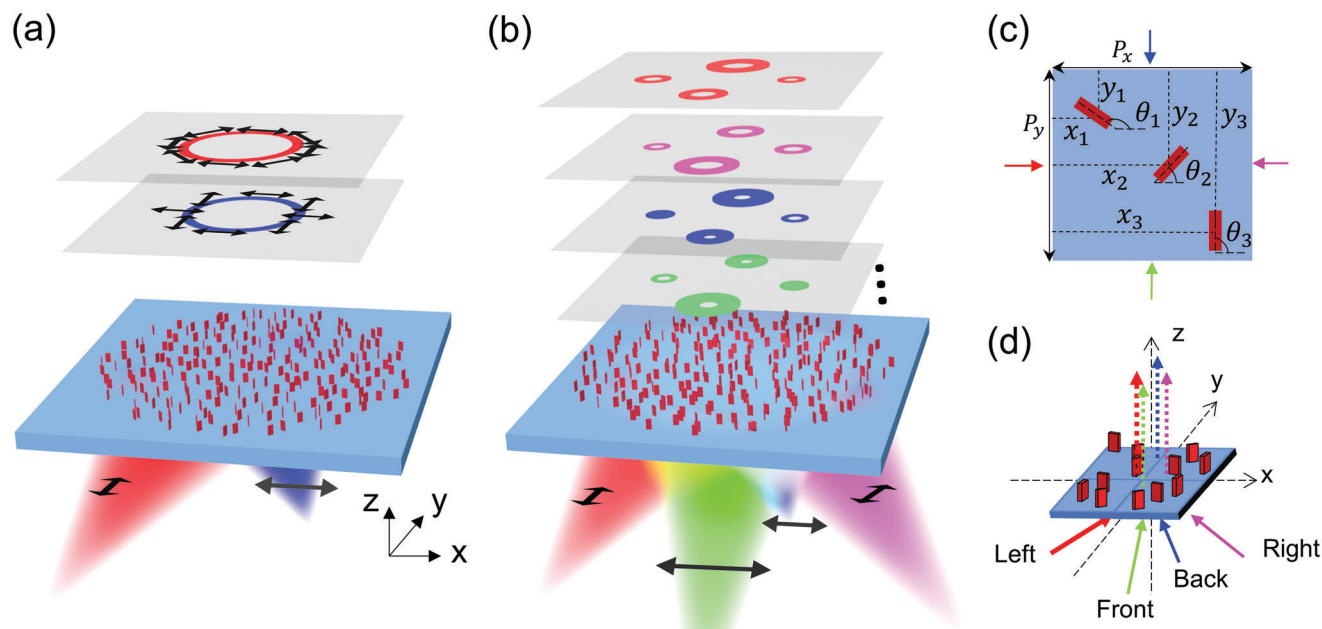OPTICAL
MATERIALS**

www.advopticalmat.de

Figure 1. a) Schematic of generation of two PPBs with left- and back-side TE incidences. The black arrows indicate the polarization direction of the incident light and the generated PPBs. b) Schematic of generation of four VVB arrays with TE light incident from four different directions. c) Geometric parameters considered in one supercell of the metasurface, including the rotation angles and locations of three nanoblocks. d) Illustration of the angle-multiplexed metasurface, which shows distinct functions when light is incident from four different directions. Pseudocolors are used in all figures for light with different angles of incidence and the corresponding complex beams for better visualization.

to the metasurfaces plane.[24,34] Combined with the AP control of multiple polarization channels enabled by the deliberate manipulation of the geometric parameters inside the supercells, the DOF of the metasurfaces can be potentially expanded and more complicated functions can be realized in a single metadevice.

In parallel to metasurfaces, structured light with complex phase-front and polarization distribution has also aroused great interest in the photonics community.[15,24,44–51] One representative example of structure light is orbital angular momentum (OAM) beams, which are paraxial beams with spiral phase profiles.[45] Due to the phase singularity at the center, OAM beams show donut-shaped intensity pattern. There are several conventional ways to produce OAM beams, including static spiral phase plate, compute-generated holography, q-plate, and spatial light modulator.[52] Owing to the unique electric field distributions and the orthogonality of OAM beams with different topological charges (TCs), they can greatly enhance the information capacity of metasurface devices. In recent decades, using metasurfaces to create the required phase distribution, researchers have realized novel applications including high-speed optical communications,[53] edge-enhancement imaging,[54] multiplex hologram,[55] and particle trapping[56] based on OAM beams with various TCs, polarizations, and frequencies. Additionally, vector vortex beams (VVBs), with spatially varying polarization and phase distributions, can be produced by overlaying OAM beams with orthogonal polarization states and various TCs. Another important variant of the VVB is perfect Poincaré beams (PPBs), which own the unique propriety of having a fixed diameter regardless of the TCs. It is anticipated that the expansion of the AP channel, once achieved, can greatly enhance the information capacity carried by various VVBs.

In this paper, by considering multiple incident directions, we propose to push the limit of the Jones matrix-based multichannel AP control even further with the assistance of GA. The key idea is to incorporate multiple Jones matrices that respond differently to the angles of incidence. Four-channel AP control of the diffracted light is realized by managing the lateral displacements as well as the rotation angles of three nanoblocks inside the supercells. Using this approach, we demonstrate the generation of structured light with space-variant polarization and phase distribution, including two PPBs, two double-ring PPBs, two PPB arrays, and four VVBs arrays, based on the AP control of four and even eight elements of the Jones matrices. Our work shows that, with the help of GA, we can precisely and inversely control the amplitude and phase at multiple channels considering different incident angles and output polarization states. Several novel applications that require the generation of on-demand structured vector vortex fields can be produced independently, which could be very challenging by the conventional design approaches. A detailed comparison between our work and previous publications regarding the functionality, degrees of freedom, design principles, and other important properties can be found in Table S1 of the Supporting Information.

2. Results and Discussions

As illustrated in **Figure 1**a, when transverse-electric (TE) light is incident from the left and back sides with a certain oblique angle, two PPBs would be generated separately. The generation of these two PPBs requires the independent AP control of four channels, i.e., the x and y polarization of the diffracted light for left- and back-side incidence. When considering the opposite incident di-

**ADVANCED
SCIENCE NEWS**

www.advancedsciencenews.com

**ADVANCED
OPTICAL
MATERIALS**

www.advopticalmat.de

rections, the AP control channels can be further expanded as the result of conjugate complex amplitudes. Figure 1b illustrates the generation of multiplexed VVB arrays when light is incident from four different directions separately. For TE incidence from the left side, a beam array containing four VVBs will be produced, each of which can be decomposed to left-handed circularly polarized (LCP) right-handed circularly polarized (RCP) light with two different sets of TCs, thanks to the independent control of the AP generation of these two polarization channels. Moreover, when light comes from the right side with the same angle of incidence, the amplitude of the diffracted light would be the same as the left-side incidence while the phase becomes the opposite value, which would lead to the conjugate far-field response. Similarly, we can produce VVB arrays with completely different TC sets using the back- and front-side incidence compared to the left- and right-side incidence cases. In the Fourier space (i.e., k space), four different VVB arrays can be observed for the four incident directions.

The supercell in our design consists of three identical silicon nanoblocks placed on a silica substrate. The width, length, and height of the nanoblock are 40, 165, and 600 nm, respectively. The rotation angles θ_1, θ_2, and θ_3, of the nanoblocks as well as their displacements along the x- and y-direction x_1, y_1, x_2, y_2, x_3, and y_3 are deliberately controlled, as shown in Figure 1c. The periodicity of the supercell P_x and P_y are fixed as 1000 nm for all of our designs in this work. Metasurfaces using a similar design have been proposed recently to achieve functions such as the generation of perfect vector vortex beams, polarization imaging, and three-channel AP control.[24–27,31,34] However, all of these works only studied the AP response of the diffracted light by fixing the angle of incidence and neglecting the displacement along the y-direction, which naturally limited the DOF in the design.

In the present work, instead of fixing the angle of incidence, we consider that light beams are incident from different directions in the full 3D space, marked as the solid arrows in four different pseudocolors (Figure 1d). The observation direction is fixed as the diffraction order perpendicular to the metasurface plane, which is marked by dashed arrows with the corresponding pseudocolors. The design principle can be understood on the basis of Jones matrix. When light is incident from the bottom air–substrate interface at the angle of $\sin^{-1}(\lambda/P_x)$ relative to the z-axis in the xz plane, or from the left-side for simplicity, the first-order diffracted light will propagate along the z-axis. The Jones matrix of the diffracted light along the normal direction can be written as[34]

$$J^l = \begin{bmatrix} J^l_{11} & J^l_{12} \\ J^l_{21} & J^l_{22} \end{bmatrix} = \begin{bmatrix} \sum_{k=1}^{n} e^{\frac{i2\pi}{P_x} x_k} \cos^2 \theta_k & \frac{1}{2} \sum_{k=1}^{n} e^{\frac{i2\pi}{P_x} x_k} \sin(2\theta_k) \\ \frac{1}{2} \sum_{k=1}^{n} e^{\frac{i2\pi}{P_x} x_k} \sin(2\theta_k) & \sum_{k=1}^{n} e^{\frac{i2\pi}{P_x} x_k} \sin^2 \theta_k \end{bmatrix} \quad (1)$$

In Equation (1), n denotes the number of nanoblocks in a supercell. For an achiral structure, the off-diagonal terms of the Jones matrix always share the same value in the linear polarization basis, that is, $J^l_{12} = J^l_{21}$. Therefore, the upper limit of the DOF in this Jones matrix is the six independent amplitude and phase values offered by J^l_{11}, J^l_{12}, and J^l_{22}, which can be controlled by θ_k and x_k, and will be optimized by GA as discussed in the following. It is worth pointing out that y_k, the displacement along the

y-direction y_k does not affect Equation (1), since this equation only involves the detour phase term $\frac{i2\pi}{P_x} x_k$. When light is incident at the angle of $\sin^{-1}(\lambda/P_y)$ relative to the z-axis in the yz plane, or from the back side for simplicity, the detour phase term will become $\frac{i2\pi}{P_y} y_k$. Therefore, another Jones matrix for the diffracted light under back-side illumination can be obtained as follows

$$J^b = \begin{bmatrix} J^b_{11} & J^b_{12} \\ J^b_{21} & J^b_{22} \end{bmatrix} = \begin{bmatrix} \sum_{k=1}^{n} e^{\frac{i2\pi}{P_y} y_k} \cos^2(\theta_k) & \frac{1}{2} \sum_{k=1}^{n} e^{\frac{i2\pi}{P_y} y_k} \sin(2\theta_k) \\ \frac{1}{2} \sum_{k=1}^{n} e^{\frac{i2\pi}{P_y} y_k} \sin(2\theta_k) & \sum_{k=1}^{n} e^{\frac{i2\pi}{P_y} y_k} \sin^2(\theta_k) \end{bmatrix} \quad (2)$$

From Equations (1) and (2), we have six independent elements, that is, J^l_{11}, $J^l_{12}(= J^l_{21})$, J^l_{22}, J^b_{11}, $J^b_{12}(= J^b_{21})$, and J^b_{22}. In this work, we focus on TE incidence, and hence we only need to consider J^l_{21}, J^l_{22}, J^b_{11}, and J^b_{12}, which determine the E_x and E_y components of the diffracted waves with TE incidence from the left- and back-sides. It is straightforward to carry out the design for transverse magnetic incidence following a similar analysis.

As shown in Figure 1d, the supercell of the designed metasurface comprises three nanoblocks in one supercell. Their locations and rotation angles, that is, $x_1, y_1, \theta_1, x_2, y_2, \theta_2, x_3, y_3$, and θ_3, represent nine variables in total, which are sufficient for us to inversely retrieve the eight DOF offered by the four complex elements (i.e., including both real and imaginary parts) in the Jones matrices of our interest. Inverse design, which starts with the desired performance and then uses a certain algorithm to generate a solution, has been widely studied in photonics. Different techniques, such as GA,[57–61] neural network,[62–66] and topology optimization,[67–70] have been applied for inverse design to implement various applications. Mimicking the process of natural evolution including selection, mutation, and crossover, GA can provide the users with optimized solutions after certain iterations. With the advantages of global optimization, inherent parallelism, and fast speed, GA has been widely applied in the inverse design for integrated photonics and planar optics.[57–61,71–73] Here, the nine structure parameters are set as the input of GA and iteratively optimized to match the four target elements in the Jones matrices to the greatest extent. A standard Python GA model has been used in our design and the details can be found in Section S2 of the Supporting Information.

As the first example, we will show the generation of two PPBs. A PPB is a vector vortex beam that can maintain a uniform ring contour with an enlarged radius along the propagation direction regardless of its TCs.[74,75] Arbitrary space-variant polarization and phase distribution can be obtained for PPBs with predefined TC combinations. Such unique characteristics are highly useful for information multiplexing, particle trapping, and optical communication. On the other hand, a perfect vortex beam (PVB), has the same proprieties as the PPB regarding the invariant annular ring shape but with homogenous polarization distribution. A PPB can be considered as the superposition of an RCP and an LCP PVB with the TC of l_m and l_n, which are located at the poles of higher-order Poincaré sphere, respectively.[51] Mathematically, a PPB can be described as

$$\left| U_N \right\rangle = \cos\left(\frac{\alpha}{2}\right) e^{\frac{i\beta}{2}} \left| \text{PVB}_R, l_m \right\rangle + \sin\left(\frac{\alpha}{2}\right) e^{-\frac{i\beta}{2}} \left| \text{PVB}_L, l_n \right\rangle \quad (3)$$

**ADVANCED
SCIENCE NEWS**

www.advancedsciencenews.com

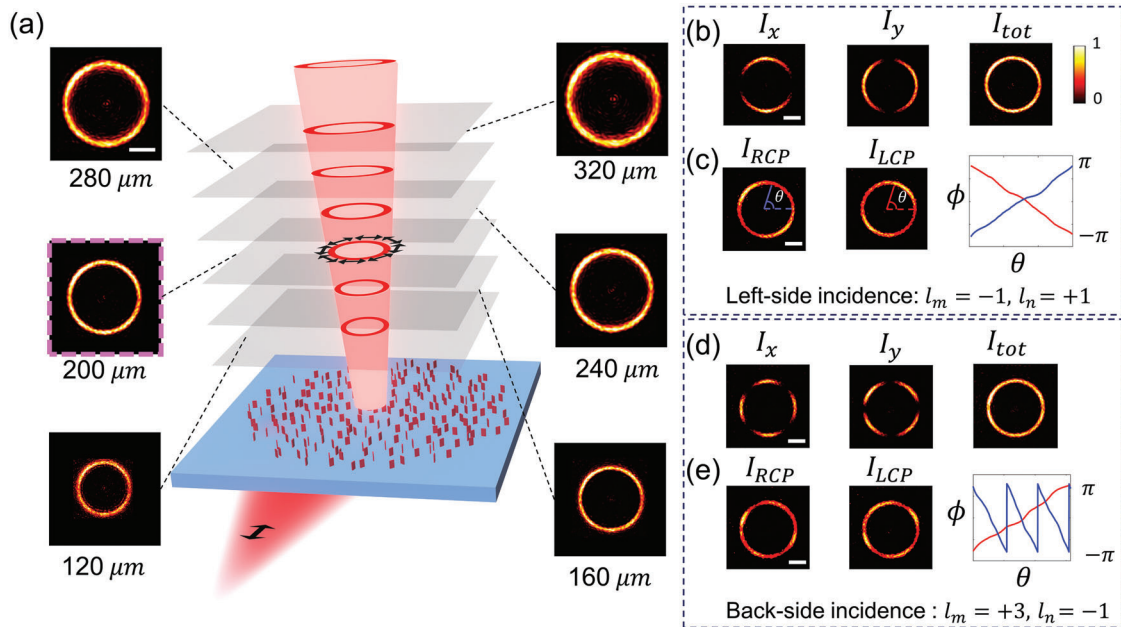**ADVANCED
OPTICAL
MATERIALS**

www.advopticalmat.de

Figure 2. a) Evolution of the intensity profile of the generated PPB along the propagation direction, when TE light is incident from the left side. The black arrows indicate the polarization state at 200 μm. b,d) Intensity profiles considering the x-, y-, and the total component of electric fields at z = 200 μm with left- and back-side incidence. c,e) Intensity profile and phase distribution along the radial direction for LCP and RCP component of electric fields with left- and back-side incidence. The blue and red lines indicate the recorded phase value ϕ versus the azimuthal angle θ along the rings for RCP and LCP components of electric fields, respectively. Scale bars: 20 μm.

Here $\cos(\alpha/2)$ and $\sin(\alpha/2)$ represent the amplitudes of the RCP and LCP components, and β is the initial phase difference between them. For simplicity, we will set $\alpha = \pi/2$ and $\beta = 0$ in all our simulations. The function of PVBs can be considered as a combination of a vortex plate, a Bessel converter, and a Fourier transformation lens. The phase profile of a PVB can be described as

$$\varphi_{PVB}(x, y) = \varphi_V(x, y) + \varphi_B(x, y) + \varphi_F(x, y) \tag{4}$$

with $\varphi_V(x, y) = l \cdot \arctan(\frac{y}{x})$, $\varphi_B(x, y) = -\frac{2\pi}{\lambda}\sqrt{x^2 + y^2} \cdot NA$, and $\varphi_F(x, y) = -\frac{\pi}{\lambda f}(x^2 + y^2)$. For the RCP and LCP components, the TC number l is denoted as l_m and l_n, respectively, while the focal distance f and numerical aperture (NA) are the same. Then, the polarization order and the phase distribution can be determined as $p = (l_m - l_n)/2$ and $l_p = (l_m + l_n)/2$. Once all the important parameters of the desired PPB, including the TCs, NA, and f are chosen, the required complex E_x and E_y components can be obtained at the metasurface plane by the conversion between circular polarization and linear polarization as $E_x = (E_L + E_R)/2$ and $E_y = (E_L - E_R)/2i$. Please note that although only the phase terms can be found for the expression of circular polarization components, the electric fields of the linear polarization components consist of complex values with both amplitude and phase information. Different from previous works that only considered rather simple functions, such as the generation of OAM beams[53] or only one single PPB,[74] to demonstrate the potential of our design method, here we aim to generate two distinct PPBs in response to two distinct directions of incidence. The two sets of the calculated complex electric fields corresponding to two different PPBs with independent combinations of l_m and l_n are fed to the GA model as the target to retrieve the locations and rotation angles of the nanoblocks.

For the first example, we demonstrate the generation of two PPBs with two incident directions. Specifically, PPB1 with $l_m = -1$ and $l_n = 1$ is generated with left-side incidence and PPB2 with $l_m = +3$ and $l_n = -1$ is generated with back-side incidence. The designed metasurface has 60×60 pixels, and the supercell at each pixel is 1000 nm × 1000 nm in size. The working wavelength is set at 650 nm. The incident angle is set as 40.5° from the bottom air–substrate interface so that the generated PPB propagates along the z-axis due to the first-order diffraction. The focal distance f is set as 200 μm and the NA is set as 0.1. We have conducted full-wave simulations by commercial software CST Microwave Suite, after the metasurfaces are inversely designed by GA. The simulation domain is 60 μm × 60 μm × 1 μm with opening boundary condition. The distribution of the electric field at the plane 1 μm above the metasurfaces is first obtained. The evolution of the electric fields around the desired distance is then calculated by the Fresnel diffraction equation to save computation memory and time. As illustrated in **Figure 2**a, for left-side incidence, we can see that the total intensity profiles of the generated electric fields maintain a stable ring shape with increasing radii along the propagation direction (from 120 to 320 μm). The electric fields at the designed working distance $z = 200$ μm for both left-side and back-side incidence are extracted and decomposed to linear and circular polarization components, as presented in Figure 2b–e. In Figure 2b,d, we can observe that the distribution of I_{tot} shows two very similar ring patterns for both left- and back-side incidence, while the decomposed intensity profiles of I_x and I_y are distinctly different, confirming the unique property of PPB.

**ADVANCED
SCIENCE NEWS**

www.advancedsciencenews.com

**ADVANCED
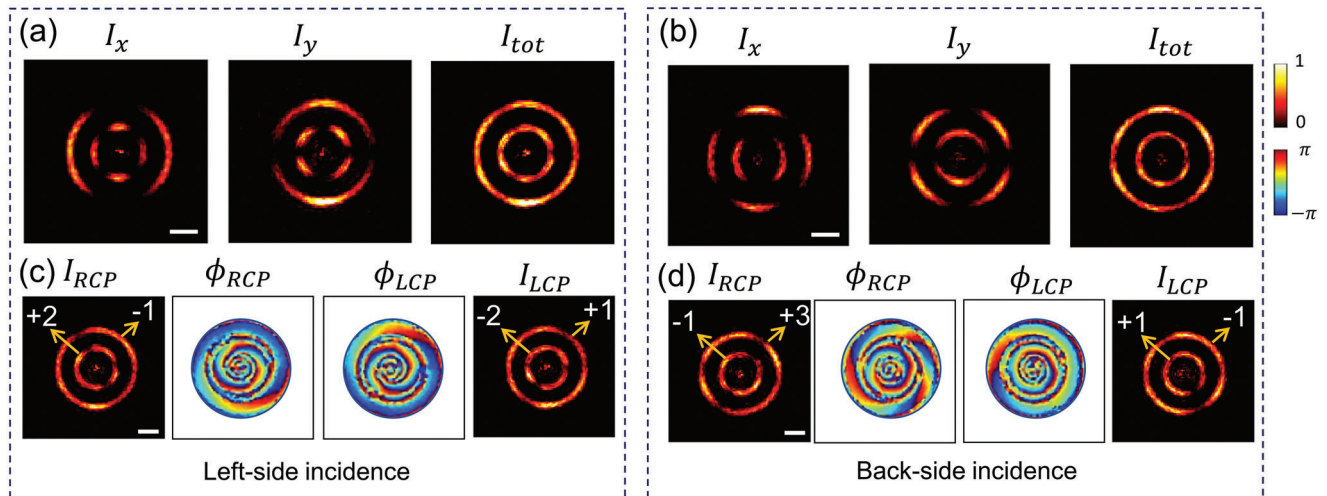OPTICAL
MATERIALS**

www.advopticalmat.de

Figure 3. a,b) Intensity profiles of the generated two independent double-ring PPBs with left- and back-side incidence. c,d) Corresponding intensity and phase profiles after the double-ring PPBs are decomposed into LCP and RCP components. The numbers in (c) and (d) denote the individual TCs. Scale bars: 10 μm.

To better understand their difference, the intensity and phase distribution along the radial direction of the decomposed LCP and RCP components are plotted in Figure 2c,e. PVBs with TCs of $l_m = -1$, $l_n = +1$, and $l_m = +3$, $l_n = -1$ for these two cases can be verified via the ring shape intensity pattern and the phase accumulation of $l \cdot 2\pi$ along the ring. The mode purities of the decomposed four PVBs are calculated as 0.94, 0.93, 0.92, and 0.94, respectively, which agree well with our expectations. The details about the calculation of the mode purity can be found in Section S3 of the Supporting Information. Moreover, the details about the simulation and the data processing are given in Section S4 of the Supporting Information.

Moreover, since the amplitude and phase of the four elements in the Jones matrix can be precisely controlled via GA, it is straightforward to realize more advanced functions. For instance, multiple-ring vector beams,[74,76,77] which consist of multiple concentric ring patterns with spatial-varied phase or polarization distributions, have been recently studied for their potential to further expand the communication channel. Combing the idea of multiple-ring vector beams with PPBs, we can further increase the DOF of the generated beams by including the ring numbers. A multiple-ring PPB can be described as a summation of multiple PPBs with different NA, which are 0.04 and 0.08 in our case. Then, by retrieving the complex amplitudes of each channel, we can generate the desired double-ring PPBs at the focal plane $f = 200$ μm. We increase the size of the metasurfaces to 90 μm × 90 μm to enhance the quality of the generated beams. As shown in **Figure 3**, the double-ring PPBs, which can be decomposed into two PVBs with $l_m = -1, +2$ and $l_n = +1, -2$ at the outer and inner rings, are produced for left-side incidence, while another double-ring PPBs with $l_m = +3, -1$ and $l_n = -1, +1$ are generated for back-side incidence. The unique patterns of the decomposed linear polarization components depicted in Figure 3a,b clearly show the absolute values of the polarization order, that is, $|p_1| = 1, 2$ and $|p_2| = 2, 1$, which are manifested by the intensity pattern of I_x and I_y In addition, the phase profiles of the circular polarization components in Figure 3c,d can verify the different

TC combinations for the two double-ring PPBs. The bright spots at the center of the generated patterns are mainly due to the focusing of the background light. Moreover, the average mode purity of the decomposed PVBs is ≈0.90. This is slightly lower than the first case since more complicated electric field distribution is involved.

To further demonstrate the advantages of our design for multichannel AP control, for the third demonstration, we will show two independent PPB arrays, each consisting of three PPBs. The required complex electric field is generated by adding up the functions for all PPBs, and a metasurface consisting of 90 × 90 pixels is designed by GA. Three PPBs, which can be decomposed to PVBs with $l_m = -1, -2, -3$ and $l_n = +1, +2, +3$, are produced for left-side incidence, while another set of PPBs with $l_m = -1$, 0, +1 and $l_n = +1, +2, +3$ are generated for back-side incidence. The unique patterns of the decomposed linear polarization components depicted in **Figure 4**a,b clearly show the absolute values of the polarization order, that is, $|p_1| = 1, 2, 3$ and $|p_2| = 1, 1, 1$. In addition, the phase profiles of the circular polarization components in Figure 4c,d can verify the different combinations of TCs for the two PPB arrays. The mode purities are calculated for all decomposed PVBs, and the average value is about 0.87. The focal distance f is set as 200 μm and the NA is set as 0.05 for all the PPBs. The detailed comparison of the complex amplitude at the metasurface plane and the intensity of the results generated from the target, GA, and FDTD simulation are given in Section S5 of the Supporting Information. Although some background noise exists for the intensity profiles of the decomposed polarization components in Figure 4, it can be further relieved when a metasurface with more pixels is used. In this work, the electric field is rigorously generated by the three functions as shown in Equation (4), which would result in a ring pattern with a rather thin width. Generally speaking, the PPB can be regarded as one kind of perfect vector vortex beams (PVVBs), whose polarization and phase are spatial-variated while the intensity patterns are independent of the TCs. Another approach to generate PVVBs but with controllable width and radius based on inverse Fresnel
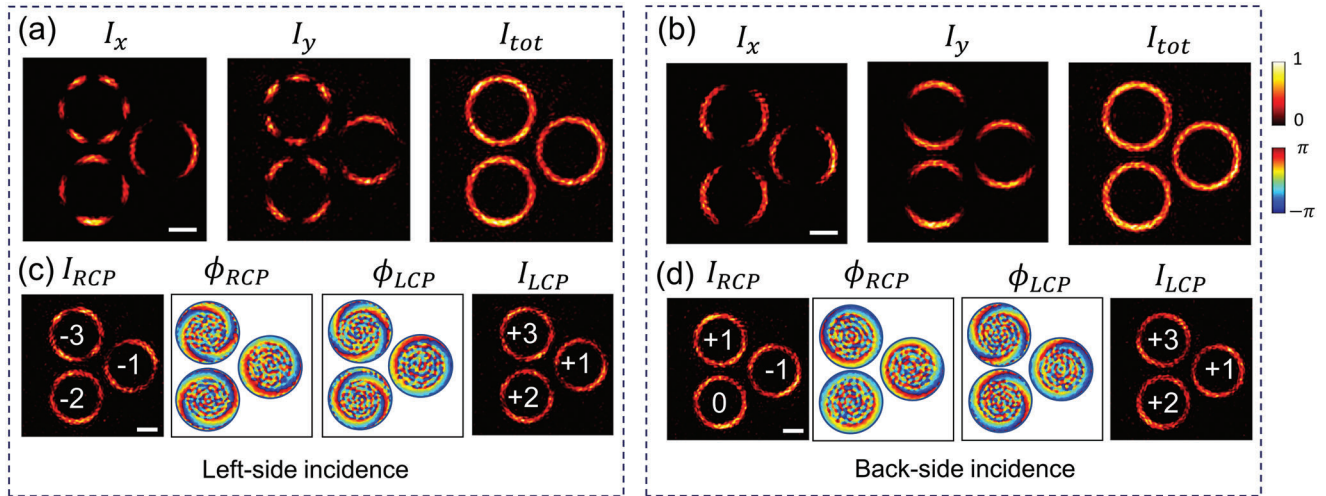
**ADVANCED
SCIENCE NEWS**

www.advancedsciencenews.com

**ADVANCED
OPTICAL
MATERIALS**

www.advopticalmat.de

Figure 4. a,b) Intensity profiles of the generated two independent PPB arrays with left- and back-side incidence. c,d) Corresponding intensity and phase profiles after the PPBs are decomposed into LCP and RCP components. The numbers in (c) and (d) denote the individual TCs. Scale bars: 10 μm.

diffraction can be found in Section S6 of the Supporting Information.

We have validated the independent control of the Jones matrix for the left-side and back-side incidence, while we can push the multiplexing capacity even further. To incorporate more Jones matrices from the existing structures, one possible solution is to change the incident angle to the opposite direction while keeping the same observation position, so that the relative displacements could be different values. If we consider that light is coming from the right or front side and still observe the beam transmitted along the positive z-direction, then the displacements x_k and y_k become $-x_k$ and $-y_k$ but the rotation angles θ_k keep the same value considering the coordinate system transformation. In this case, the Jones matrix could be rewritten as

$$J^r = \left(J^l\right)^* \tag{5}$$

$$J^f = \left(J^b\right)^* \tag{6}$$

In other words, the corresponding elements in the Jones matrix have conjugate values when light comes from the opposite direction. In this way, a Jones matrix set with four angle-dependent Jones matrices can be formed. By doubling the Jones matrices, our method can greatly enhance the functionalities of devices that work at the far field or relatively near field with certain multiplexing methods.[78,79]

For the last demonstration, we will focus on increasing the information volume carried by the generated VVBs when light is incident from four different directions. Besides the PPBs that we have discussed, VVBs, which are another type of structured light with space-variant polarization and phase distribution, have been widely applied in optical trapping,[80–82] particle acceleration,[83] and high-resolution lithography.[84–86] VVBs can be generated by the spatial overlapping of two OAM beams with different TCs as[87]

$$\left| U_N \right\rangle = \cos\left(\frac{\alpha}{2}\right) e^{\frac{i\beta}{2}} \left| \mathrm{OAM_R}, l_m \right\rangle + \sin\left(\frac{\alpha}{2}\right) e^{-\frac{i\beta}{2}} \left| \mathrm{OAM_L}, l_n \right\rangle \tag{7}$$

with $\varphi_{\mathrm{OAM}}(x, y) = \varphi_V(x, y) = l \cdot \arctan(y/x)$. For the RCP and LCP components, the TC number l is denoted as l_m and l_n, respectively. We set $\alpha = \pi/2$ and $\beta = 0$ in all our simulations for simplicity. Compared to the PPB represented by Equations (3) and (4), the generation of VVBs does not involve the Bessel function φ_B and Fourier transformation lens φ_F. Hence, the formed beams would have different ring sizes and energy densities in the far field corresponding to their TCs. Because our metasurface can create on-demand complex electric fields for both x- and y-polarized light that can greatly preserve the information needed for complex functions, four VVBs can be generated in the far field with high contrasts and low noises with left-side incidence, as demonstrated in **Figure 5**a. The metasurface consists of 80 × 80 supercells with a total size of 80 μm × 80 μm. The far-field results obtained from the full-wave simulations clearly show the characteristic intensity patterns of the x-polarization and y-polarization components, which indicate four different polarization orders $|p|$ = 1, 2, 3, 4. The phase profiles in the inset further verify the TCs of the circularly polarized components are $l_m = -1, -2, -3, -4$ and $l_n = +1, +2, +3, +4$. If the light is incident from the right side at the same angle, the amplitude profile will remain constant while the phase profile reverses the sign, resulting in the conjugate electric field in the k-space for x- and y-polarization components. As shown in Figure 5b, now we have $l_m = -2, -1, -4, -3$ and $l_n = +2, +1, +4, +3$. Since J^b is independent of J^l, we could obtain another set of VVBs when the light is incident from the back side. As shown in Figure 5c, we have $l_m = -1, 0, +1, +2$ and $l_n = +1, +2, +3, +4$. For front-side incidence presented in Figure 5d, the VVBs change to $l_m = -2, -1, -4, -3$ and $l_n = 0, +1, -2, -1$ because of the phase flipping. We can find that not only the TC sets of the LCP and RCP components are exchanged, the VVBs within one set also switch to the opposite position while their TCs flip the sign. Overall, 16 VVBs with the average mode purity of 0.85 can be generated simultaneously with four different incident directions, which can greatly benefit the applications such as optical communication and data encryption. Please note that for each incident direction, while we only consider four VVBs for the optimum simulation performance due to computational resource
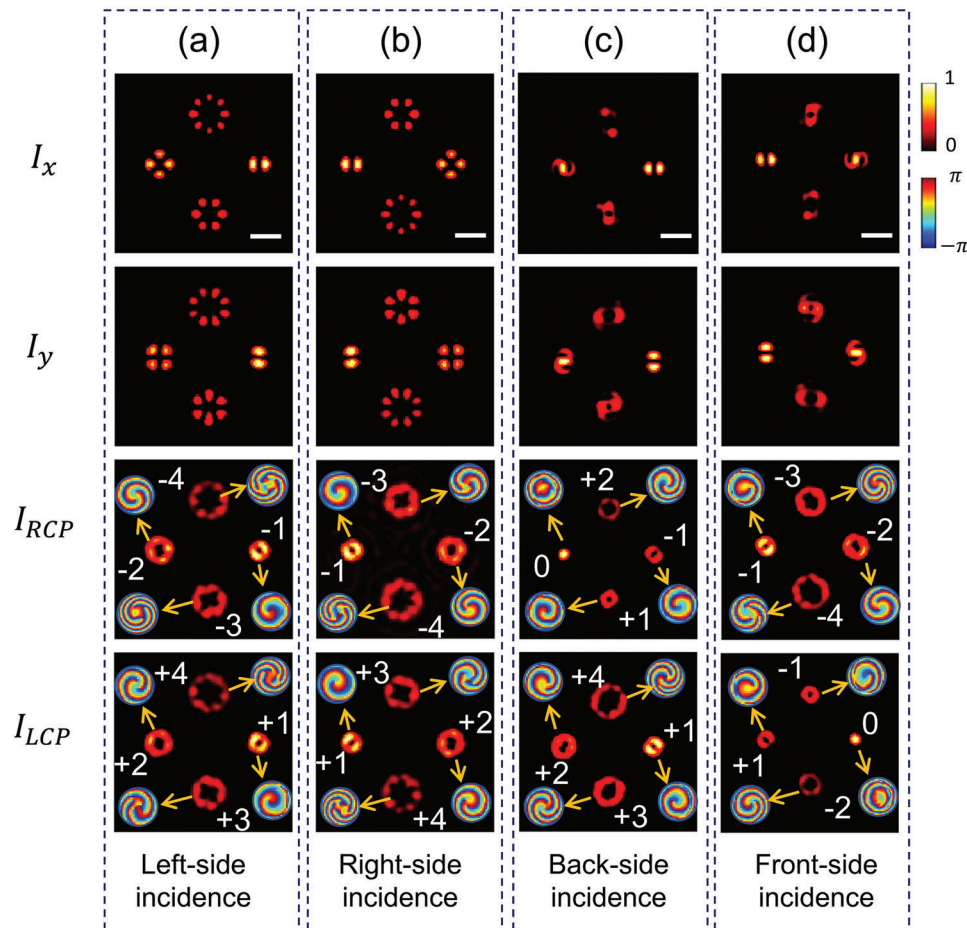
**ADVANCED
SCIENCE NEWS**

www.advancedsciencenews.com

**ADVANCED
OPTICAL
MATERIALS**

www.advopticalmat.de

Figure 5. a–d) Simulated intensity profiles of the decomposed linear polarization (top two rows), and intensity profiles of the decomposed circular polarization (bottom two rows) for the four VVB arrays, when light is incident from four different directions. The phase profiles of the OAM beams are shown in the insets. The numbers denote the individual TCs. Scale bar: 2°.

constraints, the number and order of VVBs could be further increased if enough pixels are considered during the design process to accurately recreate the required electric field distributions.

Similar to the previous works that set the input light at one specific wavelength,[24,34] where the nanoblock has the strongest scattering along the long axis, we choose 650 nm as the working wavelength for all of our simulations. The bandwidth of our devices is approximately 60 nm and the detailed discussion about the wavelength dependence of our proposed method can be found in Section S7 of the Supporting Information. For all the four designs mentioned above, the amplitudes of each pixel vary between 0 and 1, which inevitably causes low overall efficiency. Therefore, we adopt the method to make the efficiency independent of the metasurface area,[34] and the calculated efficiencies of generating the PPBs, double-ring PPBs, PPB arrays, and VVB arrays are around 10.0%, 9.3%, 8.7%, and 12.4%, which are comparable to the published works.[24,34] Please note that with the help of GA, our approach can be easily extended to other functions, structures, and even platforms. For instance, we can transfer our design method to an integrated photonics platform and realize multiple-channel manipulation of the scattered light. The details can be found in Section S8 of the Supporting Information.

3. Conclusion

In summary, we have developed a method to further increase the DOF of angle-multiplexed metasurfaces. By deliberately managing the positions and rotation angles of three nanoblocks inside a supercell, we can engineer the Jones matrices for different incident directions. With the help of GA to tune the geometric parameters, four- or even eight-channel AP control can be realized. With numerical calculation and full-wave simulation, we demonstrate two different PPBs, two double-ring PPBs and two PPB arrays generation considering two incident directions, and four VVB arrays considering four incident directions, respectively. Our method is applicable for other applications, including multichannel nanoprinting, holograms, and encryption, with appropriate designs. Ultimately, it will help to accelerate future technology development in the areas of data communication, optical manipulation, and augmented reality/virtual reality display.

Supporting Information

Supporting Information is available from the Wiley Online Library or from the author.

**ADVANCED
SCIENCE NEWS**

www.advancedsciencenews.com

**ADVANCED
OPTICAL
MATERIALS**

www.advopticalmat.de

Conflict of Interest

The authors declare no conflict of interest.

Data Availability Statement

The data that support the findings of this study are available from the corresponding author upon reasonable request.

[1] N. Yu, P. Genevet, M. A. Kats, F. Aieta, J.-P. Tetienne, F. Capasso, Z. Gaburro, *Science* **2011**, *334*, 333.
[2] N. Yu, F. Capasso, *Nat. Mater.* **2014**, *13*, 139.
[3] A. V. Kildishev, A. Boltasseva, V. M. Shalaev, *Science* **2013**, *339*, 1232009.
[4] N. Meinzer, W. L. Barnes, I. R. Hooper, *Nat. Photonics* **2014**, *8*, 889.
[5] B. Xiong, L. Deng, R. Peng, Y. Liu, *Nanoscale Adv* **2019**, *1*, 3786.
[6] J. B. Mueller, N. A. Rubin, R. C. Devlin, B. Groever, F. Capasso, *Phys. Rev. Lett.* **2017**, *118*, 113901.
[7] S. Boroviks, R. A. Deshpande, N. A. Mortensen, S. I. Bozhevolnyi, *ACS Photonics* **2017**, *5*, 1648.
[8] A. Arbabi, Y. Horie, M. Bagheri, A. Faraon, *Nat. Nanotechnol.* **2015**, *10*, 937.
[9] M. Khorasaninejad, W. T. Chen, R. C. Devlin, J. Oh, A. Y. Zhu, F. Capasso, *Science* **2016**, *352*, 1190.
[10] X. Chen, L. Huang, H. Mühlenbernd, G. Li, B. Bai, Q. Tan, G. Jin, C.-W. Qiu, S. Zhang, T. Zentgraf, *Nat. Commun.* **2012**, *3*, 1198.
[11] R. Jin, L. Tang, J. Li, J. Wang, Q. Wang, Y. Liu, Z.-G. Dong, *ACS Photonics* **2020**, *7*, 512.
[12] L. Li, K. Yao, Z. Wang, Y. Liu, *Laser Photonics Rev.* **2020**, *14*, 1900244.
[13] F. Z. Shu, J. N. Wang, R. W. Peng, B. Xiong, R. H. Fan, Y. J. Gao, Y. Liu, D. X. Qi, M. Wang, *Laser Photonics Rev.* **2021**, *15*, 2100155.
[14] N. K. Grady, J. E. Heyes, D. R. Chowdhury, Y. Zeng, M. T. Reiten, A. K. Azad, A. J. Taylor, D. A. Dalvit, H.-T. Chen, *Science* **2013**, *340*, 1304.
[15] F. Yue, D. Wen, J. Xin, B. D. Gerardot, J. Li, X. Chen, *ACS Photonics* **2016**, *3*, 1558.
[16] S. Chen, Y. Cai, G. Li, S. Zhang, K. W. Cheah, *Laser Photonics Rev.* **2016**, *10*, 322.
[17] M. Mehmood, S. Mei, S. Hussain, K. Huang, S. Siew, L. Zhang, T. Zhang, X. Ling, H. Liu, J. Teng, *Adv. Mater.* **2016**, *28*, 2533.
[18] L. Jin, Z. Dong, S. Mei, Y. F. Yu, Z. Wei, Z. Pan, S. D. Rezaei, X. Li, A. I. Kuznetsov, Y. S. Kivshar, *Nano Lett.* **2018**, *18*, 8016.
[19] B. Xiong, Y. Xu, J. Wang, L. Li, L. Deng, F. Cheng, R. W. Peng, M. Wang, Y. Liu, *Adv. Mater.* **2021**, *33*, 2005864.
[20] B. Wang, F. Dong, Q.-T. Li, D. Yang, C. Sun, J. Chen, Z. Song, L. Xu, W. Chu, Y.-F. Xiao, *Nano Lett.* **2016**, *16*, 5235.
[21] Q. H. Wang, P. N. Ni, Y. Y. Xie, Q. Kan, P. P. Chen, P. Fu, J. Deng, T. L. Jin, H. D. Chen, H. W. H. Lee, *Laser Photonics Rev.* **2021**, *15*, 2000385.
[22] Z. Li, Q. Dai, M. Q. Mehmood, G. Hu, J. Tao, C. Hao, I. Kim, H. Jeong, G. Zheng, S. Yu, *Light: Sci. Appl.* **2018**, *7*, 63.
[23] Z. Lin, X. Li, R. Zhao, X. Song, Y. Wang, L. Huang, *Nanophotonics* **2019**, *8*, 1079.
[24] Y. Bao, J. Ni, C. W. Qiu, *Adv. Mater.* **2020**, *32*, 1905659.
[25] Y. Bao, Y. Yu, H. Xu, Q. Lin, Y. Wang, J. Li, Z. K. Zhou, X. H. Wang, *Adv. Funct. Mater.* **2018**, *28*, 1805306.
[26] Z.-L. Deng, J. Deng, X. Zhuang, S. Wang, K. Li, Y. Wang, Y. Chi, X. Ye, J. Xu, G. P. Wang, *Nano Lett.* **2018**, *18*, 2885.
[27] Z. L. Deng, M. Jin, X. Ye, S. Wang, T. Shi, J. Deng, N. Mao, Y. Cao, B. O. Guan, A. Alù, *Adv. Funct. Mater.* **2020**, *30*, 1910610.
[28] S. Wang, Z.-L. Deng, Y. Wang, Q. Zhou, X. Wang, Y. Cao, B.-O. Guan, S. Xiao, X. Li, *Light: Sci. Appl.* **2021**, *10*, 24.
[29] S. Lung, K. Wang, K. Z. Kamali, J. Zhang, M. Rahmani, D. N. Neshev, A. A. Sukhorukov, *ACS Photonics* **2020**, *7*, 3015.
[30] S. Gao, C. Zhou, W. Yue, Y. Li, C. Zhang, H. Kan, C. Li, S.-S. Lee, D.-Y. Choi, *ACS Appl. Mater. Interfaces* **2021**, *13*, 14497.
[31] Y. Bao, Q. Weng, B. Li, *Laser Photonics Rev.* **2021**, 2100280.
[32] M. Liu, W. Zhu, P. Huo, L. Feng, M. Song, C. Zhang, L. Chen, H. J. Lezec, Y. Lu, A. Agrawal, *Light: Sci. Appl.* **2021**, *10*, 107.
[33] Q. Fan, M. Liu, C. Zhang, W. Zhu, Y. Wang, P. Lin, F. Yan, L. Chen, H. J. Lezec, Y. Lu, *Phys. Rev. Lett.* **2020**, *125*, 267402.
[34] Y. Bao, L. Wen, Q. Chen, C.-W. Qiu, B. Li, *Sci. Adv.* **2021**, *7*, 0365.
[35] B. Xiong, Y. Liu, Y. Xu, L. Deng, C.-W. Chen, J.-N. Wang, R. Peng, Y. Lai, Y. Liu, M. Wang, *Science* **2023**, *379*, 294.
[36] D. Lin, P. Fan, E. Hasman, M. L. Brongersma, *Science* **2014**, *345*, 298.
[37] Y. F. Yu, A. Y. Zhu, R. Paniagua-Domínguez, Y. H. Fu, B. Luk'yanchuk, A. I. Kuznetsov, *Laser Photonics Rev.* **2015**, *9*, 412.
[38] M. Kim, A. M. Wong, G. V. Eleftheriades, *Phys. Rev. X* **2014**, *4*, 041042.
[39] A. C. Overvig, S. Shrestha, S. C. Malek, M. Lu, A. Stein, C. Zheng, N. Yu, *Light: Sci. Appl.* **2019**, *8*, 92.
[40] S. M. Kamali, E. Arbabi, A. Arbabi, Y. Horie, M. Faraji-Dana, A. Faraon, *Phys. Rev. X* **2017**, *7*, 041056.
[41] S. Wan, C. Wan, C. Dai, Z. Li, J. Tang, G. Zheng, Z. Li, *Adv. Opt. Mater.* **2021**, *9*, 2101547.
[42] Z.-L. Deng, J. Deng, X. Zhuang, S. Wang, T. Shi, G. P. Wang, Y. Wang, J. Xu, Y. Cao, X. Wang, *Light: Sci. Appl.* **2018**, *7*, 78.
[43] C. Min, J. Liu, T. Lei, G. Si, Z. Xie, J. Lin, L. Du, X. Yuan, *Laser Photonics Rev.* **2016**, *10*, 978.
[44] E. Karimi, S. A. Schulz, I. De Leon, H. Qassim, J. Upham, R. W. Boyd, *Light: Sci. Appl.* **2014**, *3*, 167.
[45] Y. Shen, X. Wang, Z. Xie, C. Min, X. Fu, Q. Liu, M. Gong, X. Yuan, *Light: Sci. Appl.* **2019**, *8*, 90.
[46] Y. Liu, Y. Ke, J. Zhou, Y. Liu, H. Luo, S. Wen, D. Fan, *Sci. Rep.* **2017**, *7*, 44096.
[47] Z. Liu, Y. Liu, Y. Ke, Y. Liu, W. Shu, H. Luo, S. Wen, *Photonics Res.* **2017**, *5*, 15.
[48] H. Zhao, B. Quan, X. Wang, C. Gu, J. Li, Y. Zhang, *ACS Photonics* **2017**, *5*, 1726.
[49] F. Yue, D. Wen, C. Zhang, B. D. Gerardot, W. Wang, S. Zhang, X. Chen, *Adv. Mater.* **2017**, *29*, 1603838.
[50] H. Tan, J. Deng, R. Zhao, X. Wu, G. Li, L. Huang, J. Liu, X. Cai, *Laser Photonics Rev.* **2019**, *13*, 1800278.
[51] M. Liu, P. Huo, W. Zhu, C. Zhang, S. Zhang, M. Song, S. Zhang, Q. Zhou, L. Chen, H. J. Lezec, *Nat. Commun.* **2021**, *12*, 2230.
[52] A. M. Yao, M. J. Padgett, *Adv. Opt. Photonics* **2011**, *3*, 161.
[53] T. Lei, M. Zhang, Y. Li, P. Jia, G. N. Liu, X. Xu, Z. Li, C. Min, J. Lin, C. Yu, *Light: Sci. Appl.* **2015**, *4*, 257.
[54] P. Huo, C. Zhang, W. Zhu, M. Liu, S. Zhang, S. Zhang, L. Chen, H. J. Lezec, A. Agrawal, Y. Lu, *Nano Lett.* **2020**, *20*, 2791.
[55] H. Ren, X. Fang, J. Jang, J. Bürger, J. Rho, S. A. Maier, *Nat. Nanotechnol.* **2020**, *15*, 948.

**ADVANCED
SCIENCE NEWS**

www.advancedsciencenews.com

**ADVANCED
OPTICAL
MATERIALS**

www.advopticalmat.de

[56] Y. Ma, G. Rui, B. Gu, Y. Cui, *Sci. Rep.* **2017**, *7*, 14611.

[57] L. Shen, Z. Ye, S. He, *Phys. Rev. B* **2003**, *68*, 035109.

[58] T. Feichtner, O. Selig, M. Kiunke, B. Hecht, *Phys. Rev. Lett.* **2012**, *109*, 127701.

[59] M. D. Huntington, L. J. Lauhon, T. W. Odom, *Nano Lett.* **2014**, *14*, 7195.

[60] Z. Jin, S. Mei, S. Chen, Y. Li, C. Zhang, Y. He, X. Yu, C. Yu, J. K. Yang, B. Luk'yanchuk, *ACS Nano* **2019**, *13*, 821.

[61] L. Sanchis, A. Håkansson, D. López-Zanón, J. Bravo-Abad, J. Sánchez-Dehesa, *Appl. Phys. Lett.* **2004**, *84*, 4460.

[62] W. Ma, Z. Liu, Z. A. Kudyshev, A. Boltasseva, W. Cai, Y. Liu, *Nat. Photonics* **2021**, *15*, 77.

[63] W. Ma, F. Cheng, Y. Xu, Q. Wen, Y. Liu, *Adv. Mater.* **2019**, *31*, 1901111.

[64] W. Ma, Y. Xu, B. Xiong, L. Deng, R.-W. Peng, M. Wang, Y. Liu, *Adv. Mater.* **2022**, *34*, 2110022.

[65] D. Zhu, Z. Liu, L. Raju, A. S. Kim, W. Cai, *ACS Nano* **2021**, *15*, 2318.

[66] H. Ren, W. Shao, Y. Li, F. Salim, M. Gu, *Sci. Adv.* **2020**, *6*, 4261.

[67] D. Sell, J. Yang, S. Doshay, R. Yang, J. A. Fan, *Nano Lett.* **2017**, *17*, 3752.

[68] J. Jiang, J. A. Fan, *Nano Lett.* **2019**, *19*, 5366.

[69] O. Yesilyurt, Z. A. Kudyshev, A. Boltasseva, V. M. Shalaev, A. V. Kildishev, *ACS Photonics* **2021**, *8*, 3061.

[70] A. Y. Piggott, J. Lu, K. G. Lagoudakis, J. Petykiewicz, T. M. Babinec, J. Vučković, *Nat. Photonics* **2015**, *9*, 374.

[71] B. J. Offrein, G.-L. Bona, R. Germann, I. Massarek, D. Erni, *J. Lightwave Technol.* **1998**, *16*, 1680.

[72] D. C. Dobson, S. J. Cox, *SIAM J. Appl. Math.* **1999**, *59*, 2108.

[73] J. Hu, C.-H. Liu, X. Ren, L. J. Lauhon, T. W. Odom, *ACS Nano* **2016**, *10*, 10275.

[74] H. Mao, Y.-X. Ren, Y. Yu, Z. Yu, X. Sun, S. Zhang, K. K. Wong, *Photonics Res.* **2021**, *9*, 1689.

[75] D. Li, S. Feng, S. Nie, C. Chang, J. Ma, C. Yuan, *J. Appl. Phys.* **2019**, *125*, 073105.

[76] Z. Mou, C. Zhou, P. Lu, Q. Yue, S. Wang, S. Teng, *Photonics Res.* **2021**, *9*, 2125.

[77] Z. Nie, Z. Li, G. Shi, X. Zhang, Y. Wang, Y. Song, *Opt. Lasers Eng.* **2014**, *59*, 93.

[78] Q. Wei, L. Huang, X. Li, J. Liu, Y. Wang, *Adv. Opt. Mater.* **2017**, *5*, 1700434.

[79] L. Huang, H. Mühlenbernd, X. Li, X. Song, B. Bai, Y. Wang, T. Zentgraf, *Adv. Mater.* **2015**, *27*, 6444.

[80] J. Ng, Z. Lin, C. T. Chan, *Phys. Rev. Lett.* **2010**, *104*, 103601.

[81] M. Li, S. Yan, Y. Liang, P. Zhang, B. Yao, *Phys. Rev. A* **2017**, *95*, 053802.

[82] Y. Zhang, J. Shen, C. Min, Y. Jin, Y. Jiang, J. Liu, S. Zhu, Y. Sheng, A. V. Zayats, X. Yuan, *Nano Lett.* **2018**, *18*, 5538.

[83] Y. Liu, D. Cline, P. He, *Nucl. Instrum. Methods Phys. Res., Sect. A* **1999**, *424*, 296.

[84] R. Dorn, S. Quabis, G. Leuchs, *Phys. Rev. Lett.* **2003**, *91*, 233901.

[85] M. Kang, J. Chen, X.-L. Wang, H.-T. Wang, *J. Opt. Soc. Am. B* **2012**, *29*, 572.

[86] T. Bauer, S. Orlov, U. Peschel, P. Banzer, G. Leuchs, *Nat. Photonics* **2014**, *8*, 23.

[87] F. Cardano, E. Karimi, S. Slussarenko, L. Marrucci, C. de Lisio, E. Santamato, *Appl. Opt.* **2012**, *51*, C1.